Waveform Inversion in Ultrasound Tomography from Homogeneous Starting Models

Rehman Ali*, Trevor Mitcham*, Melanie Singh†, Brenna Harris*, Madalina Tivarus*, Nebojsa Duric*†
Department of Imaging Sciences, University of Rochester Medical Center, Rochester, NY, USA *
Department of Biomedical Engineering, University of Rochester, Rochester, NY, USA †
Email: Rehman_Ali@URMC.Rochester.edu, Trevor_Mitcham@URMC.Rochester.edu, melaniesingh@rochester.edu, Brenna_Harris@URMC.Rochester.edu, Madalina_Tivarus@URMC.Rochester.edu, Nebojsa_Duric@URMC.Rochester.edu

2023 IEEE International Ultrasonics Symposium (IUS) | 979-8-3503-4645-9/23/$31.00 ©2023 IEEE | DOI: 10.1109/IUS51837.2023.10307870

***Abstract*—While waveform inversion is the clinical gold standard for obtaining high-resolution images of sound speed and attenuation in tissue, it was long assumed that bent ray tomography was necessary to obtain a starting model, especially with a ring array transducer. However, recent works show that waveform inversion is possible with a reasonable choice of homogeneous starting models and sufficiently low-frequency content in the waveform to avoid cycle skipping. In the case of transcranial imaging, we cannot afford to use a bent ray tomography because it quickly becomes unstable in the presence of a highly refractive skull. We examine the parameters that would enable waveform inversion to image the soft tissue in the brain through the high sound speed and attenuation in the skull.**

***Index Terms*—Waveform Inversion, Ultrasound Tomography, Transcranial Imaging**

I. Introduction

Ultrasound Tomography (UST) is an emerging imaging modality that provides CT-like reconstructions using ultrasound pulses instead of X-rays. It has gained acceptance for breast imaging and the FDA has recently approved it for adjunctive screening of women with dense breast tissue [1]. UST is capable of tissue-specific imaging and characterization, by virtue of its transmission ultrasound capability [2], [3] and use of full waveform inversion (FWI). The intrinsic image sequences generated by UST consist of (i) sound speed, related physically to tissue density, (ii) attenuation, relating to tissue stiffness when combined with sound speed and (iii) reflection imaging which provides anatomical information.

The current form of UST is a direct consequence of how the concept evolved in the development of a breast imaging system. Initially, UST was developed based on a compromise in frequencies to accommodate both reflection (B-mode) imaging and transmission-based FWI imaging, the former requiring high frequencies for better resolution and the latter requiring low frequencies for the convergence of FWI, leading to the development of a broadband 3 MHz center frequency ring transducer [4]. Despite the fact that FWI specifically requires sub-MHz frequencies, which lie at the tail-end of spectrum, FWI generates clinically relevant high-resolution images [1], [3]. Compounding over many transmitters (1024) and receivers (1024) allows FWI to overcome the low signal-to-noise ratios in the individual measurements [3], [4].

While waveform inversion is the clinical *in-vivo* gold standard for obtaining high-resolution diagnostic-quality images of the speed of sound in breast tissue [2], [3], the convergence of waveform inversion in ultrasound tomography is heavily impacted by the choice of starting model [5]. Ray tomography is often used as the starting model for waveform inversion; however, artifacts resulting from ray tomography can continue to persist during waveform inversion. On the other hand, a homogeneous starting model for waveform inversion may result in cycle skipping artifacts if the frequency of the transmitted waveform is too high or the error between the starting model and ground-truth is too large.

In the case of transcranial UST imaging, we cannot afford to use bent ray tomography due to instabilities created by the presence of a highly refractive skull. In this work, we choose to completely eliminate the dependence on ray models to provide a starting model and use simulations to understand the optimal configuration for transcranial UST imaging. The biggest challenge in applying UST to brain imaging is the large contrast in sound speed between bone and soft brain tissue, which results in cycle skipping artifacts [5]. One way to overcome cycle skipping is to lengthen the cycle by using lower frequencies.

II. Theory and Methods

A. FWI Using the Helmholtz Equation

Using finite difference methods [6], we solve the 2D Helmholtz equation to obtain a pressure field $\mathbf{u}$ for a given source δ, frequency $\omega = 2\pi f$, and slowness $\mathbf{s}$ (i.e., the reciprocal of sound speed):

$$(\nabla^2 + \omega^2 \mathbf{s}^2)\mathbf{u}(\omega, \mathbf{s}) = \delta(\omega), \tag{1}$$

After discretization, the $(\nabla^2 + \omega^2 \mathbf{s}^2)$ operator becomes a sparse matrix A that encodes the finite difference scheme so that equation (1) can be described using the following matrix-vector formulation (where $\mathbf{u}$ and δ are now vectors over spatial locations on the discretized grid):

$$A(\omega, \mathbf{s})\mathbf{u}(\omega, \mathbf{s}) = \delta(\omega), \tag{2}$$

Differentiating both sides of this equation with respect to s gives us:

$$\frac{\partial \mathbf{u}}{\partial \mathbf{s}} = -A^{-1}\frac{\partial A}{\partial \mathbf{s}}\mathbf{u} = -A^{-1}\frac{\partial A}{\partial \mathbf{s}}A^{-1}\delta, \tag{3}$$

Rather than observing the full pressure field $\mathbf{u}$ at all locations in space, we only observe the pressure field $\mathbf{p}$ at the ring array. The relationship between $\mathbf{p}$ and $\mathbf{u}$ is: $\mathbf{p} = K\mathbf{u}$, where K is a sampling operator that extracts the pressure field at each element of the ring array. The relationship between changes in slowness and changes in the simulated pressure field at the ring array is

$$\frac{\partial \mathbf{p}}{\partial \mathbf{s}} = -KA^{-1}\frac{\partial A}{\partial \mathbf{s}}\mathbf{u} = -KA^{-1}\frac{\partial A}{\partial \mathbf{s}}A^{-1}\delta, \tag{4}$$

The cost function for FWI is:

$$\begin{aligned} E(\omega, \mathbf{s}) &= \frac{1}{2}\sum_{i=1}^{N} \|\mathbf{p_i}(\omega, \mathbf{s}) - \mathbf{p_{obs,i}}(\omega)\|_2^2 = \\ &\frac{1}{2}\sum_{i=1}^{N} \left(\mathbf{p_i}(\omega, \mathbf{s}) - \mathbf{p_{obs,i}}(\omega)\right)^H \left(\mathbf{p_i}(\omega, \mathbf{s}) - \mathbf{p_{obs,i}}(\omega)\right), \end{aligned} \tag{5}$$

where $\mathbf{p_i}$ and $\mathbf{p_{obs,i}}$ are the simulated and observed pressure measurements on the ring array for the i^{th} single-element transmission $\delta_\mathbf{i}$ (i ranges from 1 to N, the number of elements on the ring array). The gradient of $E(\omega, \mathbf{s})$ with respect to slowness $\mathbf{s}$ is given by:

$$\begin{aligned} \nabla_\mathbf{s} E &= \sum_{i=1}^{N} Re\left\{\left(\frac{\partial \mathbf{p_i}}{\partial \mathbf{s}}\right)^H (\mathbf{p_i} - \mathbf{p_{obs,i}})\right\} = \\ &-\sum_{i=1}^{N} Re\left\{\left(\frac{\partial A}{\partial \mathbf{s}}\mathbf{u_i}\right)^H (A^H)^{-1}K^T (\mathbf{p_i} - \mathbf{p_{obs,i}})\right\}, \end{aligned} \tag{6}$$

To implement the conjugate gradient method for this objective function, we also need a linear estimate of the perturbation in the pressure field $\Delta\mathbf{p_i}$ for a given perturbation $\mathbf{d_k}$ to the slowness.

$$\begin{aligned} \Delta\mathbf{p_i} &= \left(\frac{\partial \mathbf{p_i}(\omega, \mathbf{s})}{\partial \mathbf{s}}\right)\mathbf{d_k} = \\ &-KA(\omega, \mathbf{s})^{-1}\left(\frac{\partial A(\omega, \mathbf{s})}{\partial \mathbf{s}}\mathbf{u_i}(\omega, \mathbf{s})\right)\mathbf{d_k}. \end{aligned} \tag{7}$$

This perturbation $\Delta\mathbf{p_i}$ allows us to properly scale the search direction $\mathbf{d_k}$ and update the slowness model $\mathbf{s_k}$:

$$\alpha_k = -\frac{\mathbf{d_k}^T \nabla_\mathbf{s} E}{\|\Delta\mathbf{p_i}\|_2^2} \tag{8}$$

$$\mathbf{s_{k+1}} = \mathbf{s_k} + \alpha_k \mathbf{d_k} \tag{9}$$

Note that first iteration of conjugate gradient is simply direct gradient descent (i.e., $d_1 = -\nabla_\mathbf{s} E(\omega, \mathbf{s})$).

B. Complex-Valued Source Scaling

The FWI described in the previous section assumes that the correct phase and amplitude is used for each single-element source $\delta_\mathbf{i}$; however, in practice, the phase and amplitude of each source must be estimated from the measured waveform. The following projection formula provides a complex scaling γ_i that accounts for both the amplitude and phase from each source i:

$$\gamma_i = \frac{\mathbf{p_i}^H \mathbf{p_{obs,i}}}{\mathbf{p_i}^H \mathbf{p_i}} \tag{10}$$

The source vector and pressure fields are scaled to $\{\delta_\mathbf{i} \rightarrow \gamma_i \delta_\mathbf{i}\}$, $\{\mathbf{u_i} \rightarrow \gamma_i \mathbf{u_i}\}$, and $\{\mathbf{p_i} \rightarrow \gamma_i \mathbf{p_i}\}$, respectively.

C. Experimental Methods

Hounsfield units from an X-Ray CT of the head were mapped onto sound speed, density, and attenuation values obtained from the literature [7], yielding a morphologically and acoustically accurate model (Figure 1). A hematoma was added to the model to create the final sound speed, density, and attenuation models shown in Figure 1. The data acquisition system was simulated using the k-Wave software package [8] and consisted of a 1024 element ring transducer, 22cm in diameter to match the characteristics of transducer available in our lab (similar to the ones used for breast imaging). The emission (1 MHz center frequency; 75% fractional bandwidth), propagation, and reception of sound waves was simulated using the head model as the medium. These simulations generated numerical RF data that were then processed and reconstructed using our current FWI-based breast UST algorithm. FWI was performed from either 300 or 100 KHz to 600 kHz in 10 kHz steps.

III. Results and Discussion

Figure 2(a) shows the true sound speed simulated in k-Wave with the ring transudcer, skull, brain tissue, and hematoma identified. In Figure 2(b), the FWI algorithm used a starting frequency of 300 kHz (to simulate the lowest usable frequency in our current hardware system) and a final frequency of 600 kHz to achieve the desired resolution of approximately 1mm. However, strong cycle skipping artifacts generated by the skull obscure the brain tissue. If our hardware could generate and record signals down to 100 kHz, Figure 2(c) shows that most of these cycle-skipping artifacts would disappear. Keeping in mind that the algorithms used in this pilot study were originally developed for breast imaging, it is not surprising that some artifacts remain. The large contrast between bone and soft tissue underscores the need for customized algorithms and hardware to address the cycle skipping artifacts.

In seismic imaging literature, one strategy to overcome cycle skipping is adaptive waveform inversion (AWI) [9]. AWI is a time-domain algorithm that involves constructing impulse responses that convert simulated waveforms into actual measurements. While conventional FWI is based on directly minimizing the error between simulations and measurements, AWI reconstructs the sound speed image by driving these impulse responses towards zero-time lag. As a result, AWI completely circumvents cycle skipping; however, it requires a broadband implementation to model the impulse responses.

A major artifact that remains in Figure 2(c), despite overcoming the majority of cycle skipping, is the overestimation of skull thickness and the underestimation of sound speed in the skull. The ground truth sound speed contrast between the clot and ventricles is 110 m/s and the estimated contrast is 117.8+/-10.2 m/s. While the hematoma is well reconstructed, the sound speed within the skull is underestimated by roughly 600 m/s, and skull thickness is overestimated by roughly 2x.

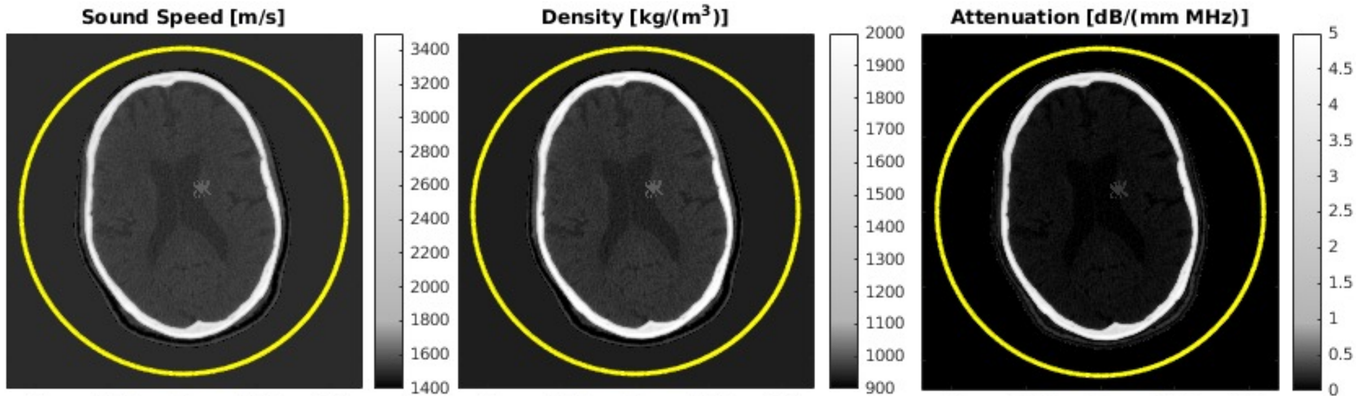

Fig. 1. Sound speed, density, and attenuation maps used for k-Wave simulation of transcranial UST. Transducer elements are shown in yellow.

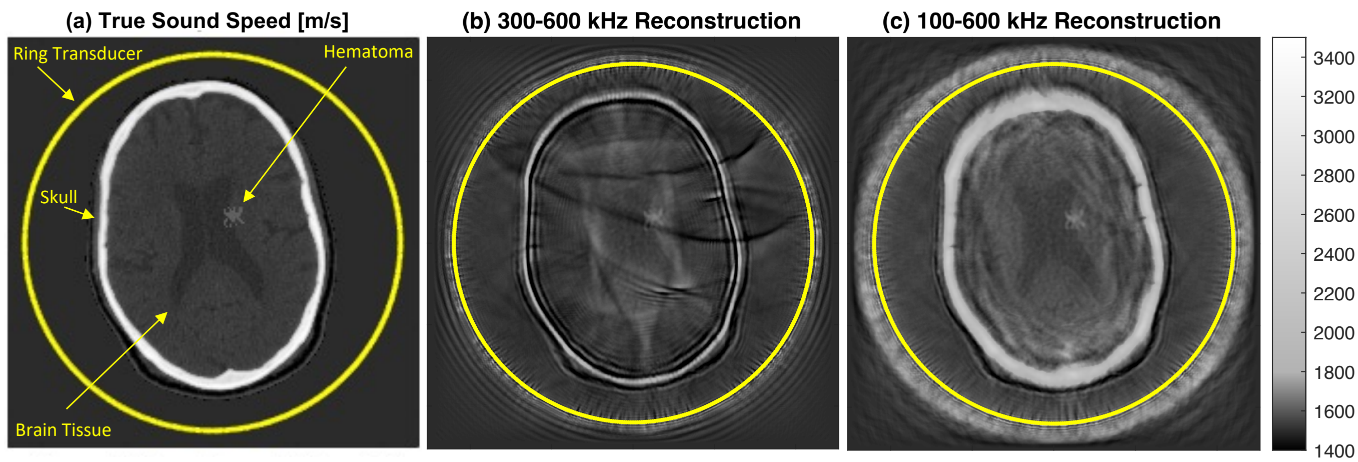

Fig. 2. (a) Numerical model of skull, brain, and a focal hematoma. (b) The first reconstructed image (result of FWI from 300 to 600 kHz) shows strong cycle-skipping artifacts that obscure much of the brain tissue and overlap with the injury site. (c) Lowering the starting frequency of FWI to 100 kHz greatly reduces cycle-skipping artifacts.

This effect is largely due to 1) the high contrast between skull and brain tissue, and 2) using low frequencies to overcome cycle skipping. The high contrast between the skull and brain tissue resulted in the cycle skipping seen in Figure 2(b). In order to overcome cycle skipping, we needed to perform FWI at lower frequencies. However, the result of using lower frequencies is a lower resolution reconstruction. As a result, the skull is estimated as a lower sound speed compared to its true value over a thicker region. To better resolve the sharp contrast between bone and soft tissue, it may be necessary to use prior knowledge about the sound speed in bone to develop a two-compartment model [10], [11] where the interfaces between bone and soft tissue are estimated.

IV. Conclusions and Future Work

We demonstrate that it may be possible to use full waveform inversion (FWI) without ray tomography for transcranial ultrasound tomography (UST) by relying on sufficiently low frequency content. The results of this work will inform future hardware development as well as algorithm considerations for this new application of UST. Although simulations show that cycle skipping may be overcome by using sufficiently low frequencies in FWI, the same low-frequency FWI is responsible for underestimating the sound speed in the skull while also overestimating the thickness of the skull.

Acknowledgment

We would like to acknowledge the key clinical insights from Drs. Derrek Schartz, Redi Rahmani, Matthew Bender, Edward Vates, and Deborah Rubens that motivated this study. This work was funded by University of Rochester Medical Center and the National Institute of Biomedical Imaging and Bioengineering (NIBIB) under grants F32-EB034589 and R01-EB028652.

References

[1] M. Yamashita, R. F. Brem, L. Baker, T. F. Mahoney, P. Walker, R. M. Treat, and L. H. Larsen, "Abstract p3-04-13: Patient experience with automated softvue 3d whole breast tomographic ultrasound," *Cancer Research*, vol. 83, no. 5_Supplement, pp. P3–04, 2023.

[2] J. Wiskin, B. Malik, R. Natesan, D. Borup, N. Pirshafiey, M. Lenox, and J. Klock, "Full wave 3d inverse scattering transmission ultrasound tomography: breast and whole body imaging," in *2019 IEEE International Ultrasonics Symposium (IUS)*. IEEE, 2019, pp. 951–958.
[3] G. Sandhu, C. Li, O. Roy, S. Schmidt, and N. Duric, "Frequency domain ultrasound waveform tomography: breast imaging using a ring transducer," *Physics in Medicine & Biology*, vol. 60, no. 14, p. 5381, 2015.
[4] N. Duric, C. Li, O. Roy, and S. Schmidt, "Acoustic tomography: promise versus reality," in *2011 IEEE International Ultrasonics Symposium*. IEEE, 2011, pp. 2033–2041.
[5] R. Ali, T. Mitcham, and N. Duric, "Impact of starting model on waveform inversion in ultrasound tomography," in *Medical Imaging 2023: Ultrasonic Imaging and Tomography*, vol. 12470. SPIE, 2023, pp. 89–98.
[6] Z. Chen, D. Cheng, W. Feng, and T. Wu, "An optimal 9-point finite difference scheme for the helmholtz equation with pml." *International Journal of Numerical Analysis & Modeling*, vol. 10, no. 2, 2013.
[7] T. D. Webb, S. A. Leung, J. Rosenberg, P. Ghanouni, J. J. Dahl, N. J. Pelc, and K. B. Pauly, "Measurements of the relationship between ct hounsfield units and acoustic velocity and how it changes with photon energy and reconstruction method," *IEEE transactions on ultrasonics, ferroelectrics, and frequency control*, vol. 65, no. 7, pp. 1111–1124, 2018.
[8] B. E. Treeby and B. T. Cox, "k-wave: Matlab toolbox for the simulation and reconstruction of photoacoustic wave fields," *Journal of biomedical optics*, vol. 15, no. 2, p. 021314, 2010.
[9] M. Warner and L. Guasch, "Adaptive waveform inversion: Theory," *Geophysics*, vol. 81, no. 6, pp. R429–R445, 2016.
[10] J. Fincke, X. Zhang, B. Shin, G. Ely, and B. W. Anthony, "Quantitative sound speed imaging of cortical bone and soft tissue: Results from observational data sets," *IEEE Transactions on Medical Imaging*, vol. 41, no. 3, pp. 502–514, 2021.
[11] P. Marty, C. Boehm, and A. Fichtner, "Shape optimization for transcranial ultrasound computed tomography," in *Medical Imaging 2023: Ultrasonic Imaging and Tomography*, vol. 12470. SPIE, 2023, pp. 77–88.